Cyclobutane-linked Nanothreads through Thermal and Photochemically Mediated Polymerization of Cyclohexadiene

Morgan Murphy,[a] Bohan Xu,[b] Katie E. Rank,[c] Sikai Wu,[a] Steven Huss,[a] John V. Badding,[abd] Steven A. Lopez,[c] Vincent H. Crespi,[abd] and Elizabeth Elacqua[a*]

[a.] *Department of Chemistry, The Pennsylvania State University, University Park, PA, 16802. Email: elizabeth.elacqua@psu.edu*
[b.] *Department of Physics, The Pennsylvania State University, University Park, PA, 16802.*
[c.] *Department of Chemistry and Chemical Biology, Northeastern University, Boston, MA, 02115.*
[d.] *Department of Materials Science and Engineering, The Pennsylvania State University, University Park, PA, 16802.*

Supporting Information

Synthetic Procedures

1,3-Cyclohexadiene (1,3-diene) Pressure-Induced Polymerization: Liquid 1,3-diene was loaded into a diamond anvil cell (DAC) and closed to avoid evaporation of the sample (P = 1-2 GPa). There are no reports of a low-temperature or high-pressure crystal structure for 1,3-diene, and the sample would only solidify as an amorphous solid upon loading. The high-pressure reactivity of 1,3-diene was explored in a DAC using in situ vibrational spectroscopy. Scans of the sample were taken approximately every 2 GPa. The samples were compressed over a period of 7-9 hours and held at 21 GPa overnight. Upon decompression, the recovered solid is transparent and appears dark under cross-polarizers.

1,4-Cyclohexadiene (1,4-diene) Pressure-Induced Polymerization: Liquid 1,4-diene was loaded into a DAC and was closed to avoid evaporation of the sample (P = 1-2 GPa). Here, a polycrystalline solid was formed and compressed to a maximum of 21 GPa. Attempts to grow single crystals through annealing at low pressure or cooling still resulted in polycrystalline samples. Powder samples were formed by cycles of partially melting and pressurizing polycrystals. Using two gas membranes and a digital gas controller (Druck PACE5000) samples were compressed at rates of approximately 0.1 GPa/min. After reaching the maximum pressure of 21 GPa, the samples were held overnight. Samples were decompressed at the same rate of 0.1 GPa/min. Upon decompression, a white off-white solid is recovered.

1,4-Cyclohexadiene Photochemically Mediated Pressure-Induced Polymerization: Liquid 1,4-diene was loaded into a DAC and was closed to avoid evaporation of the sample (P = 1-2 GPa). Polycrystalline samples were used for these experiments. Methods introducing UV irradiation for a specific amount of time at various pressure points or continuous UV light exposure throughout slow compression were investigated. Experiments which used three hours of broadband UV irradiation at the maximum pressure (18, 16, 14, 12, and 10 GPa) in the experiment afforded the most crystalline solids. The samples were exposed to broadband UV irradiation for a total of 3 hours at the maximum pressure, with a Raman scan after each hour. After irradiation, samples were decompressed to ambient pressure where an off-white solid was recovered. Recovered samples from these experiments to 14, 15, and 18 GPa produced semi-crystalline solids. The 12 and 10 GPa samples did not diffract or revered to liquids, respectively.

1,4-Cyclohexadiene Paris Edinburgh Press Synthesis: Bulk samples were compressed in a V7 Paris-Edinburgh (PE) press equipped with double-toroidal polycrystalline diamond anvils. The press was operated through an automated oil syringe pump allowing for controlled pressure and hold times.1,4-diene was sealed in cupped stainless-steel gaskets by freezing droplets on the anvils in liquid nitrogen and quickly transferring samples to the PE press. Proper precautions need to be taken in order to safely load and compress liquids when working with anvils with liquid nitrogen to avoid shattering of anvils and pieces potentially becoming projectile in nature. Sample was compressed and decompressed at the following rates: 1.5 mL/min up to 250 bar; 0.07 mL/min to 500 bar and held for 30 min; 0.03 mL/min to 940 bar held between 360 and 1440 min. Approximately 8 mg of a white solid was recovered.

Experimental Methods

Raman Spectroscopy: All Raman spectra were collected using a Renishaw inVia Raman spectrometer, with a microscope attachment, using a 633 nm laser excitation source. A 20x long working distance objective was utilized to focus on the sample through the top diamond. To limit sample damage, a laser power of 100 µW was used. Experiments with UV irradiation utilized the same Renishaw inVia Raman spectrometer. The 20x long working distance objective was used to focus the Hg mercury lamp on the sample for the duration of UV irradiation.

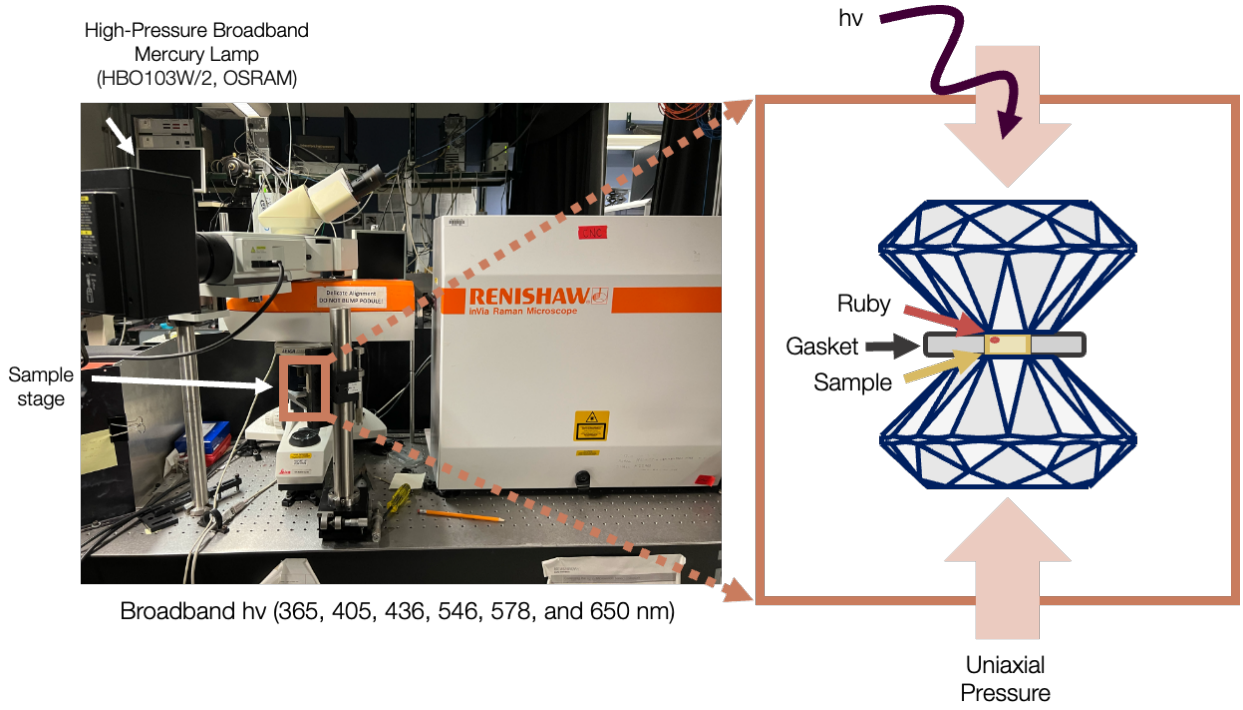

Scheme S1. UV lamp setup with Raman microscope for photochemistry experiments in diamond cells

Recovered IR Spectroscopy: Infrared spectra of recovered gasket samples were obtained using a Bruker Vertex70 spectrometer with a Hyperion 3000 FT-IR microscope and MCT detector. With the same sample experimental conditions, background spectra were taken and subtracted from the sample spectra using OPUS software.

In situ IR Spectroscopy: In situ IR spectra were collected at Brookhaven National Lab, using the National Synchrotron Light Source facilities at 22-IR-1. Spectra for 1,3-diene and 1,4-diene were obtained in a DAC using a Bruker Vertex 80v FT-IR spectrometer coupled with a Hyperion-2000 microscope and MCT detector. An initial background scan was taken and subtracted from each sample spectra, each with 512 scans, a resolution of 4 cm^{-1}, and a range of 500-4000 cm^{-1}. DAC samples were prepared for IR spectroscopy with KBr which was utilized as a pressure-transmitting media and to prevent sample over-saturation.

PE Infrared Spectroscopy: FT-IR spectra of bulk nanothread samples were obtained using a Bruker Vertex70 spectrometer with a Hyperion 3000 FT-IR microscope and MCT detector. With the same sample experimental conditions, background spectra were taken and subtracted from the sample spectra using OPUS software.

Recovered Gasket XRD: X-ray diffraction measurements were completed at the Advanced Photon Source (APS) in Argonne National Lab. Recovered gasket samples and DAC samples were probed at HPCAT using the 16-BM-D beamline. A 22 keV 5 × 5 μm monochromatic beam was used and a Pilatus 1M-F detector was used for data collection. Samples that diffracted were also rotated to ensure no diffraction was blocked by the detector or beam stop.

In situ synchrotron XRD: In situ powder diffraction was collected by rastering over a 40 x 40 μm with an omega rotation of ± 10 degrees and 10-minute exposure time. Single crystal diffraction was collected with a 22 keV 5 × 5 μm monochromatic beam with a Pilatus 1M-F detector and was taken over an omega rotation of ± 20 degrees with 1 degree per step.

The collected 2-dimensional patterns for gasket samples and in situ experiments were processed into 1-dimensional data using DIOPTAS diffraction software.[1]

PE Press X-Ray Diffraction: Rigaku X-ray equipment with a high flux rotating anode X-ray source (MicroMax 007HF), optics (Virimax-VHF), goniometer (universal 4-circle kappa), and detector (HyPix-Arc 150˚) were used. Individual crystals were measured using powder scans with 300 second exposure times

Polarized Light Microscopy: Recovered gasket samples were analyzed under polarized light to explore birefringence. An Olympus BX61 optical microscope with 20x objective was used. Polarized samples were taken with the sample between crossed polarizers. A full 530 nm waveplate was used to enhance the polarization images.

X-Ray Photoelectron spectroscopy: XPS experiments were performed using a Physical Electronics VersaProbe III instrument equipped with a monochromatic Al kα x-ray source (hν = 1,486.6 eV) and a concentric hemispherical analyzer. Charge neutralization was performed using both low energy electrons (<5 eV) and argon ions. The binding energy axis was calibrated using sputter cleaned Cu (Cu $2p_{3/2}$ = 932.62 eV, Cu $3p_{3/2}$ = 75.1 eV) and Au foils (Au $4f_{7/2}$ = 83.96 eV).[2] Peaks were charge referenced to CH_x band in the carbon 1s spectra at 284.8 eV. Measurements were made at a takeoff angle of 45° with respect to the sample surface plane. This resulted in a typical sampling depth of 3-6 nm (95% of the signal originated from this depth or shallower). Quantification was done using instrumental relative sensitivity factors (RSFs) that account for the x-ray cross section and inelastic mean free path of the electrons. On homogeneous samples major elements (>5 atom%) tend to have standard deviations of <3% while minor elements can be significantly higher. The analysis size was ~200μm in diameter.

Differential Scanning Calorimetry: A Discovery DSC (TA instruments) was used to collect measurements. A sample mass of 0.7 mgs was used. After equilibration at 30.00 °C, a ramp rate of 20 ˚C/min to 275 ˚C for 3 cycles.

Thermogravimetric Analysis: A Discovery TGA 550 with autoloader (TA instruments) was used to collect measurements. Samples mass of 2-4 mg was used for measurements. Samples were run from 25-1000 ˚C under a nitrogen atmosphere at a ramp rate of 10 C˚/min.

Gas Chromatography - Mass Spectrometry: GC-MS (electron impact, EI) spectra were recorded on Agilent 8890 GC and 5977B Series MSD systems. The sample was partially soluble in benzene-d_6 and run in the deuterated solvent.

High-Pressure Behavior of 1,3-Cyclohexadiene

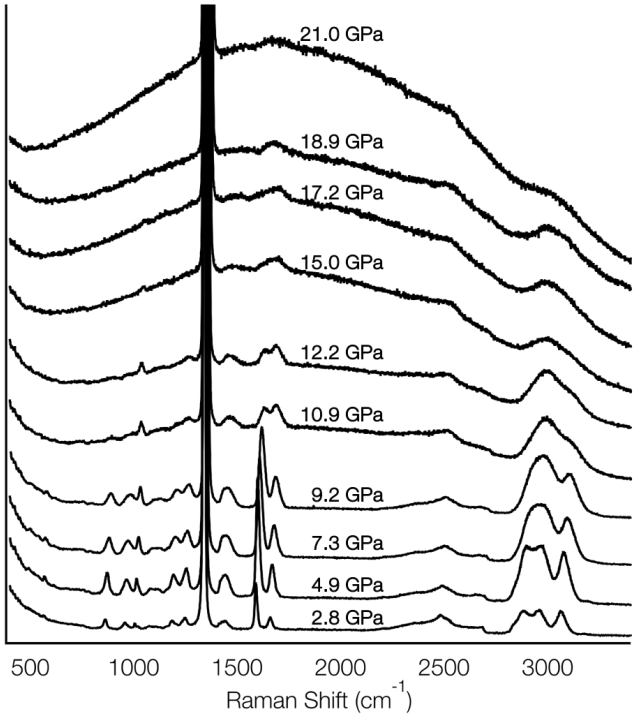

Figure S1. In situ Raman spectroscopy for the compression of 1,3-diene to 21 GPa. An increase in the photoluminescent background at 10.9 GPa suggest the onset of a chemical reaction. The broad peaks suggest an amorphous sample throughout compression.

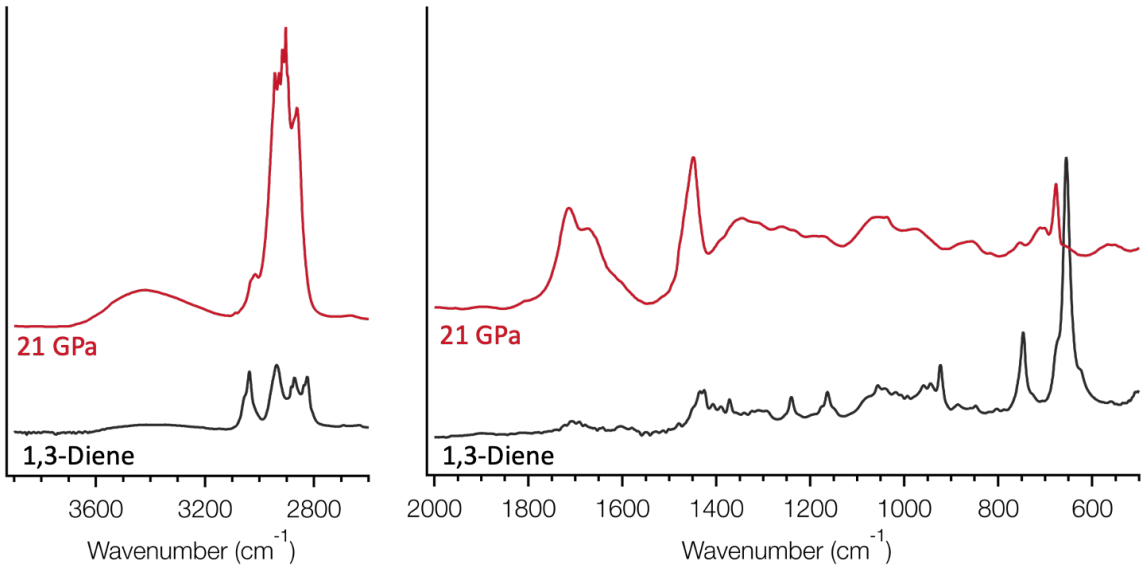

Figure S2. IR spectrum of 1,3-diene liquid sample (black) and compression to 21 GPa (red). The sharp features in the C—H stretching region in the recovered gasket sample oversaturated the detector at approximately 3000 cm^{-1}.

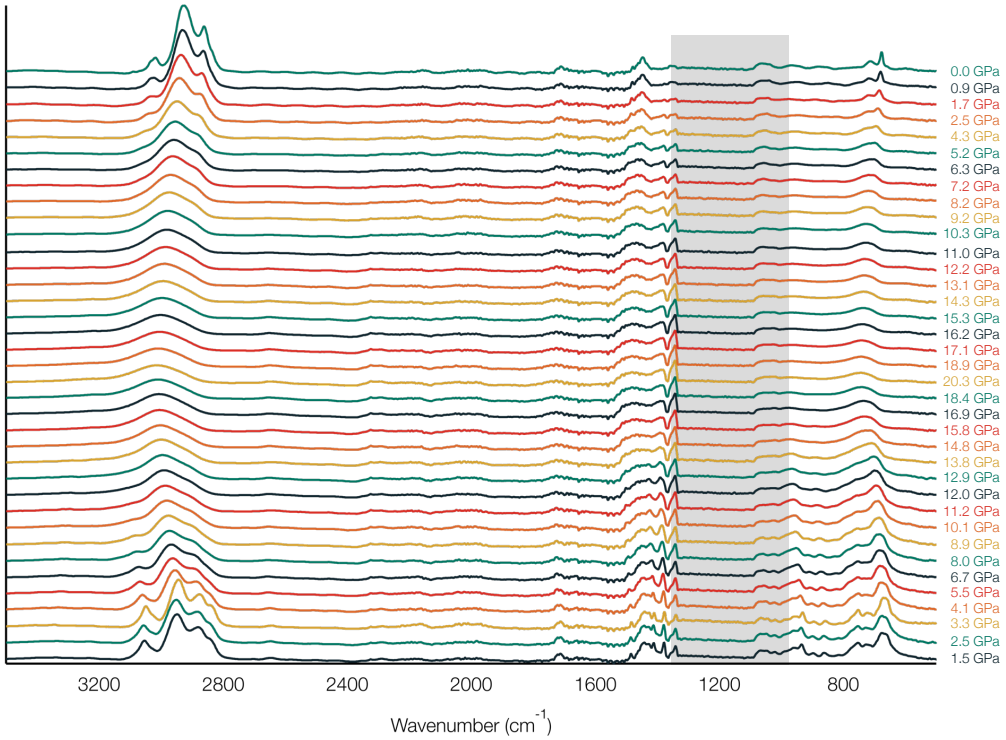

Figure S3. In situ IR spectroscopy of 1,3-diene to 20 GPa shows the reactivity of the sample under pressure and the formation of a highly saturated product. The gray area indicates diamond from the DAC.

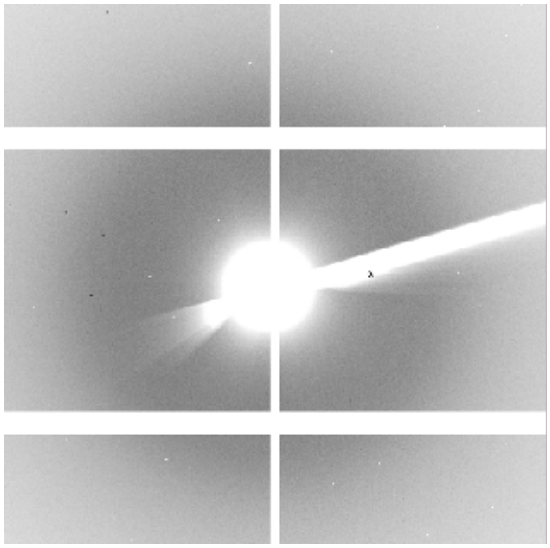

Figure S4. Diffraction of recovered gasket sample of 1,3-diene compressed to 21 GPa. The lack of diffraction suggests recovery of an amorphous sample.

Supplemental Experimental Figures for 1,4-Cyclohexadiene-Derived Threads

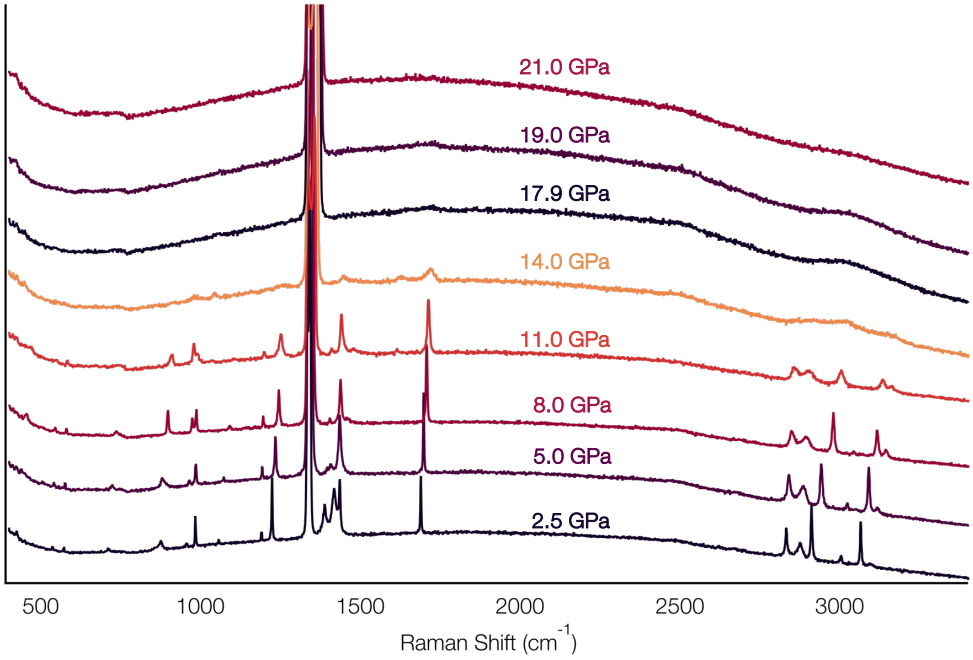

Figure S5. In situ Raman spectroscopy for the compression of 1,4-diene to 21 GPa.

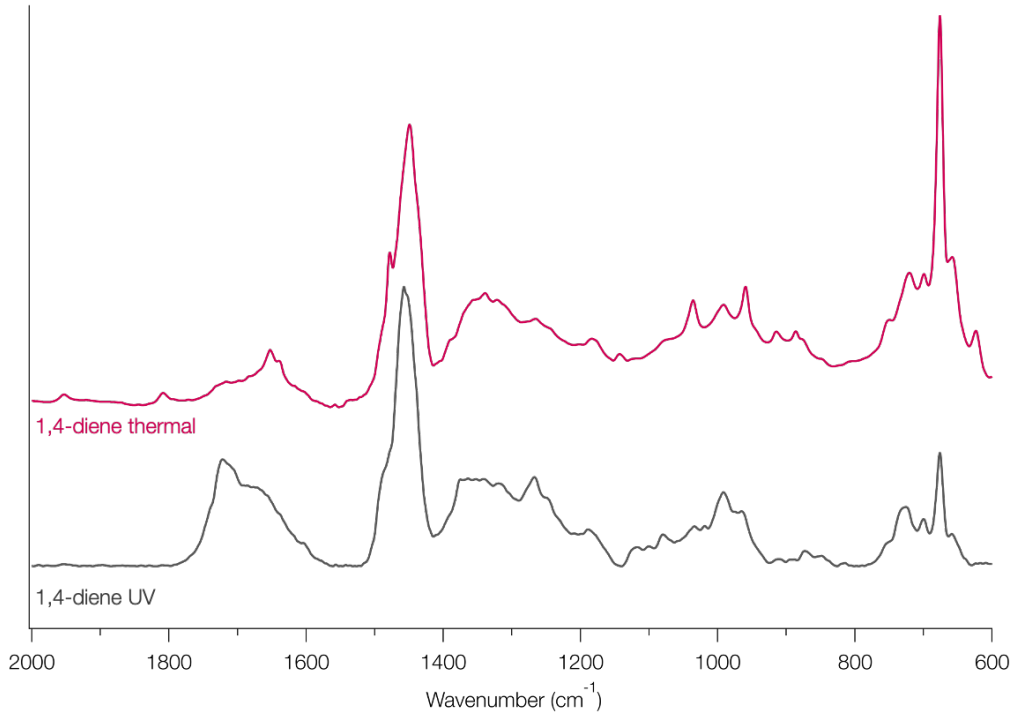

Figure S6. IR spectrum of 1,4-diene thermal (black) and photochemical (red) compressions.

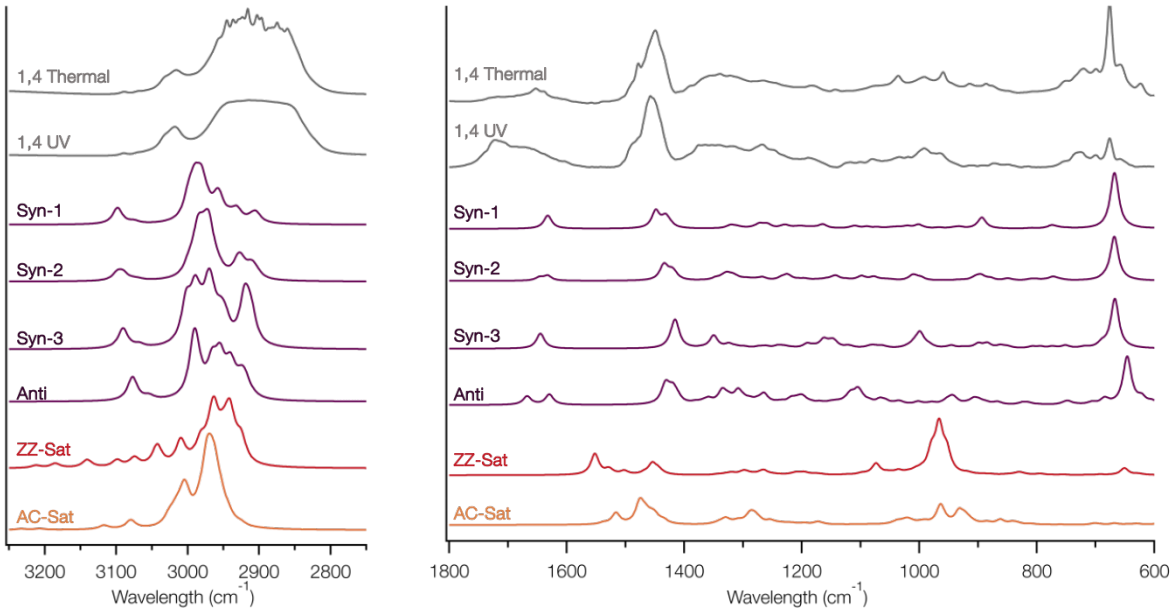

Figure S7. Recovered gasket IR spectra for 1,4-diene compared to the simulated spectra for various nanothread types. Experimental traces for thermal compression to 21 GPa and UV compression to 18 GPa are shown in gray. Simulated IR spectra for the CB-*syn* or CB-*anti* (purple), ZZ-sat (red), and AC-sat (orange) are shown. Sharp peaks in the C—H stretching region of the photochemically-derived sample are due to oversaturation of the detector and could not be avoided.

The IR spectra for polymerization products with and without UV are very similar. The experimental spectra each share rather sharp peaks at 600 cm^{-1} which are seen in the simulated spectra of the cyclobutane-linked threads and ZZ-sat structures. One difficulty in identifying a structure from the IR spectra arises from overlapping vibrational modes in the cyclobutane and cyclohexane rings. As these are similar in vibrational frequency and are fused together, the signals overlap and cannot be used to further identify a product.

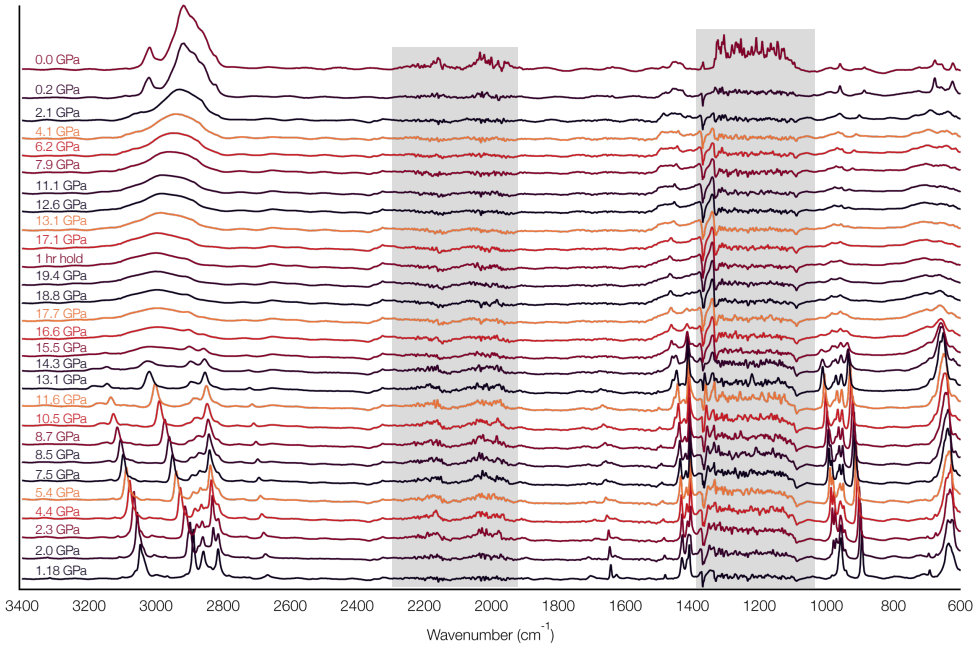

Figure S8. In situ IR spectroscopy of 1,4-diene to 19 GPa shows the reactivity of the sample under pressure and the formation of a highly saturated product. Gray areas indicate diamond from the DAC.

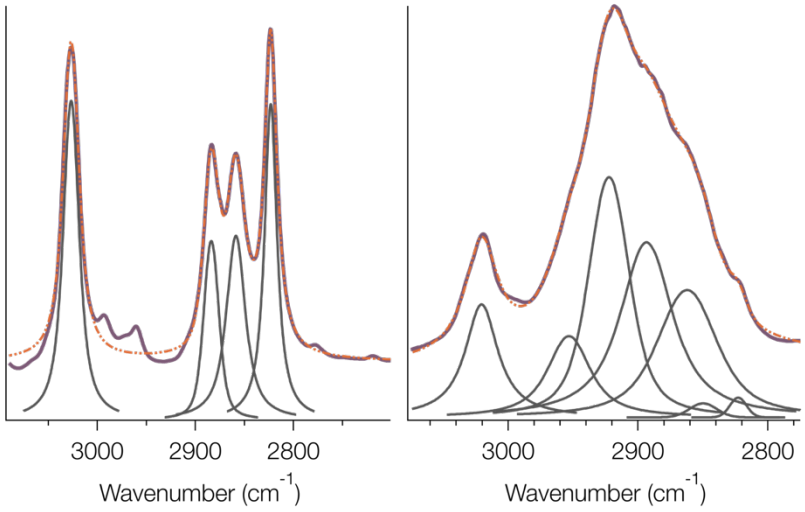

Figure S9. IR spectra of the C—H stretching region of 1,4-diene (left) starting material and (right) product recovered from compression to 21 GPa. Purple traces are experimental data, gray is the deconvoluted peaks, and orange is the fit.

For a better understanding of the C—H stretching region we used an established approach to semi-quantitatively determine the abundance of C(sp^3) vs C(sp^2) content of the samples. With integrated areas of the starting material (0 GPa) and recovered product (compressed to 21 GPa, recovered to 0 GPa) the C—H stretching areas were converted to areas of C(sp^3) and C(sp^2) with a previously reported working

curve.[3] Molecular 1,4-cyclohexadiene has 6 carbon atoms in which 2 carbons (33%) are expected to be sp^3 hybridized. Our analysis slightly overestimates the C(sp^3) abundance in the starting material at 39%. In the product recovered from 21 GPa suggest a value of 80% C(sp^3) abundance in the recovered sample. While only a semi-quantitative approach, our analysis suggests a much higher C(sp^3) content in the recovered material which is attributed to a reaction under pressure.

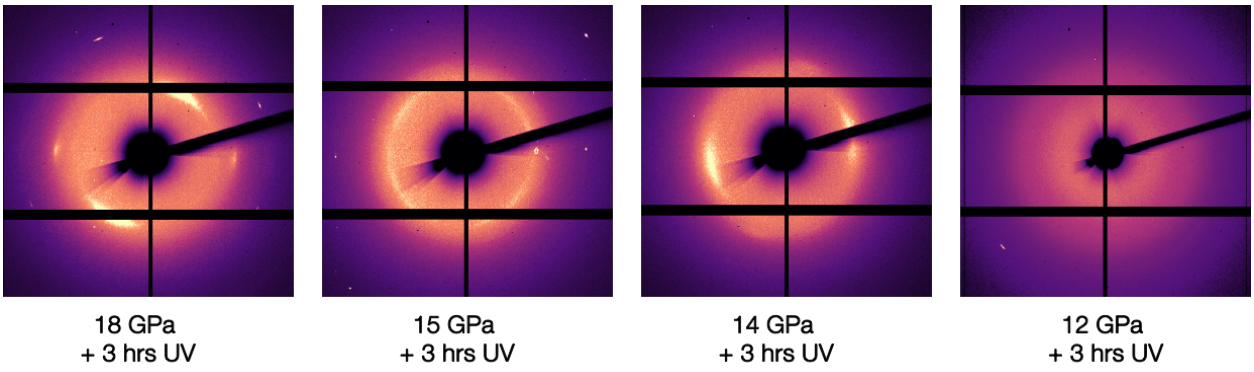

Figure S10. Diffraction from recovered gasket samples of 1,4-diene compressed to various maximum pressures where samples were exposed to UV light.

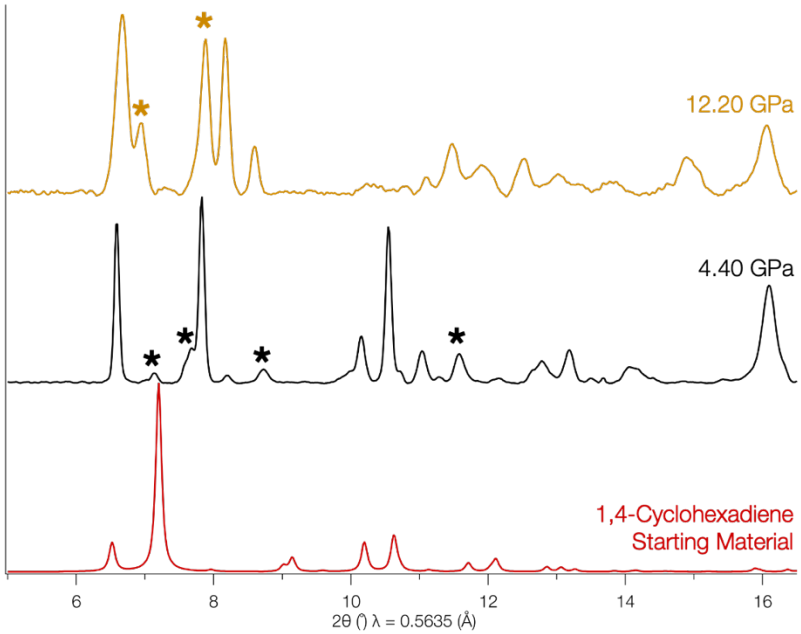

Figure S11. PXRD of the cyclohexadiene starting material (red), high-pressure phase at 4.40 GPa (black), and start of reaction at 12.2 GPa (yellow). New peaks are indicated suggesting a new phase at 4.4 GPa and formation of a product at 12.2 GPa.

Computational Methods: Packings of 1,4-Cyclohexadiene-Derived Threads and X-ray Diffraction

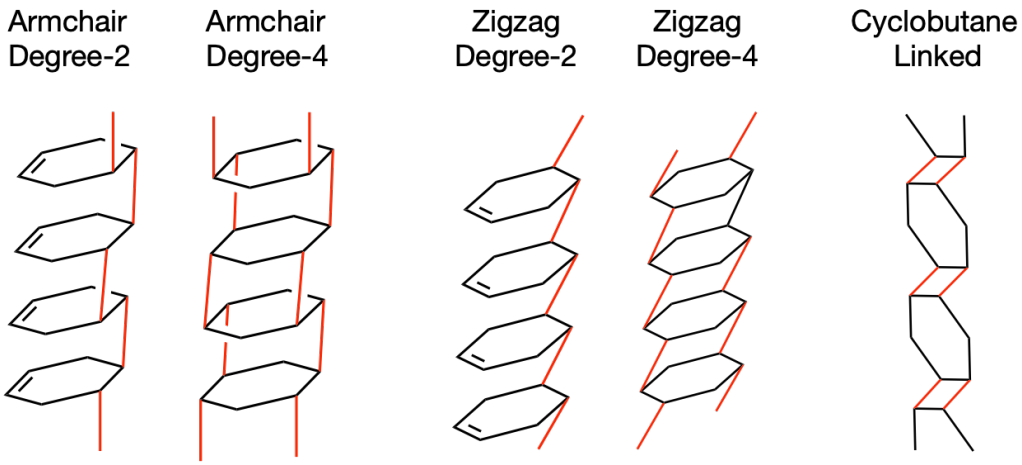

Figure S12. Structures of potential 1,4-diene-derived nanothread structures. Bonds shown in red are those responsible for linking the rings (propagation).

Structures of crystalline threads packings are relaxed through first principle computation with PBE functional, DFT-D3/BJ Van der Waals correction, and plane wave basis set, implemented through code package VASP. All possible threads with axial periodicity less than or equal to two precursor molecules and without significant across-cell-strain are considered in the simulations. The bending strain of Cyclobutane-linked (CB) threads can be understood by the orientations of the hydrogen atoms. Consider the viewing direction normal to the direction of any double bond that was saturated during reaction, and orient the thread vertically. The number of hydrogen atoms oriented to the left side of the thread, must equal the number of hydrogen atoms oriented to the right side, for the thread to have no significant bending strain. The types of considered threads are shown above in Scheme S1 and in the main text Figures 4 and 5. Armchair Degree-4 is abbreviated as AC-Sat. Zigzag Degree-4 is abbreviated as ZZ-Sat. Cyclobutane-linked threads have names such as CB-Anti-A and CB-Syn-2 explained in the main text.

In short, the total number of simulated to-be-relaxed thread packings is #species×2×8, where #species is the number of distinct thread chemical species. There are 2 kinds of unit cells (a cell with 20 Å × 20 Å along the two packing dimensions and a cell whose two packing dimensions are derived from experimental data). There are 8 kinds of reflection relation between the two threads in one unit cell.

In more detail, we assume there are two threads in a unit cell. For each thread species, the following systematic search of thread packing was carried out.

- The first kind of unit cell is derived from the three experimental *d*-spacings. One unit cell vector is along the thread direction while the other two unit cell vectors are derived from the three experimental quasi-hexagonal *d*-spacings with the assumption that there are two threads in the unit cell. This cell is then slightly isotopically expanded by a factor of 1.2 along packing directions so two threads can fit into the cell without overlapping.
- The second kind of unit cell that is 20 Å × 20 Å along the two packing directions. One unit cell vector is along the thread direction while the other two unit cell vectors are set to be 20 Å with 90 degrees in between. 20 Å × 20 Å is a mostly-neutral pre-relaxation cell size that is large enough to fix two threads in one such unit cell.

For each thread species and each unit cell, two threads are placed in the unit cell. One is fixed and eight possible reflections on the second thread are indicated by Ref000, Ref001, Ref010, Ref011, Ref100, Ref101, Ref110, Ref111. For instance, Ref000 means no reflection is applied on the second thread. Ref100 means a reflection that inverts x direction is applied on the second thread. Ref111 means three reflections that invert x y and z are applied on the second thread. After the application of reflections, both threads in the unit cell are rotated by a random angle between 0 and 180 degrees.

The initial structures with the first kind of unit cell (the experimentally derived unit cell) are geometrically relaxed first with a fixed unit cell so threads can rotate into orientations that are the most consistent with experimental cell. Then the cells are allowed to be relaxed under 19.9 GPa by density function theory through VASP. The initial structures with the second kind of unit cell (the 20 Å × 20 Å unit cell) are relaxed at 19.9 GPa with changeable unit cell directly. [001] is the thread direction. [110], [110], and MaxRealDspacing([020], [200]) are reliably identified as the three *d*-spacings corresponding to the quasi-hexagonal packing.

The final structure .cif files, poscar files, *d*-spacing .csv files, and enthalpies are available as SI. Structures with names including “ECell” refers to structures whose pre-relaxation unit cells are those from the experimental data. Structures with names including “RCell” refers to structures whose pre-relaxation unit cells are the 20 Å × 20 Å cells.

The results of packing exhaustion are summarized in Figures S13 and S14.

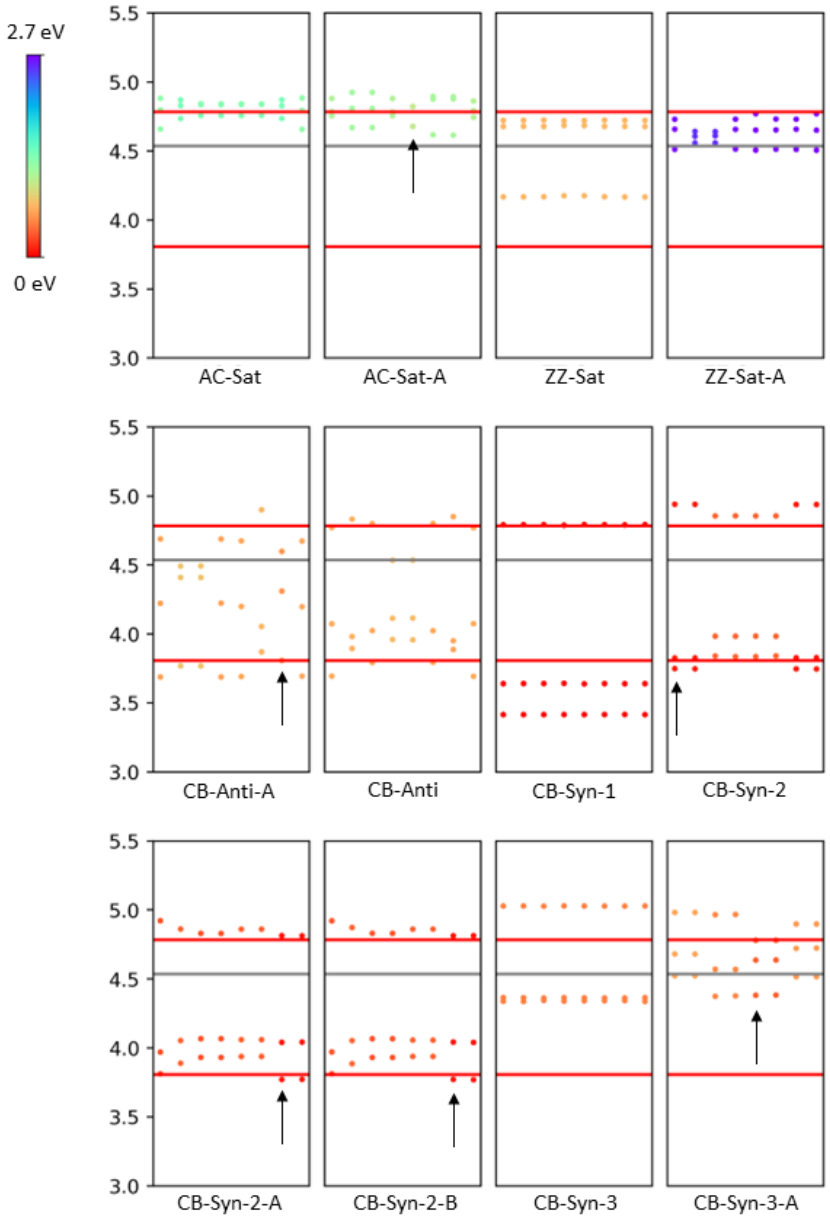

Figure S13. Packing of 1,4-diene-derived thread structures that start with a pre-relaxation unit cell consistent with the three experimentally observed *d*-spacings at 19.9 GPa. The grey line shows the experimental *d*-spacing that likely belongs to the precursor molecular crystal (hollow triangle in the main text figures). Simulated thread with lowest enthalpy at 20 GPa is colored red. The thread with highest enthalpy, colored as violet, is 2.7eV per molecule higher than the lowest enthalpy packing. Within each plot, *i.e.,* each chemical species, the *d*-spacings of 8 simulated packings are displayed. Each black arrow points to the lowest enthalpy packing among the same chemical species. Some chemical species, such AC-Sat, do not have the black arrow in this figure, because its lowest packing is found in the packing simulation that start with the 20 Å × 20 Å cell in the next figure, instead of the experimentally derived cell shown in the current figure.

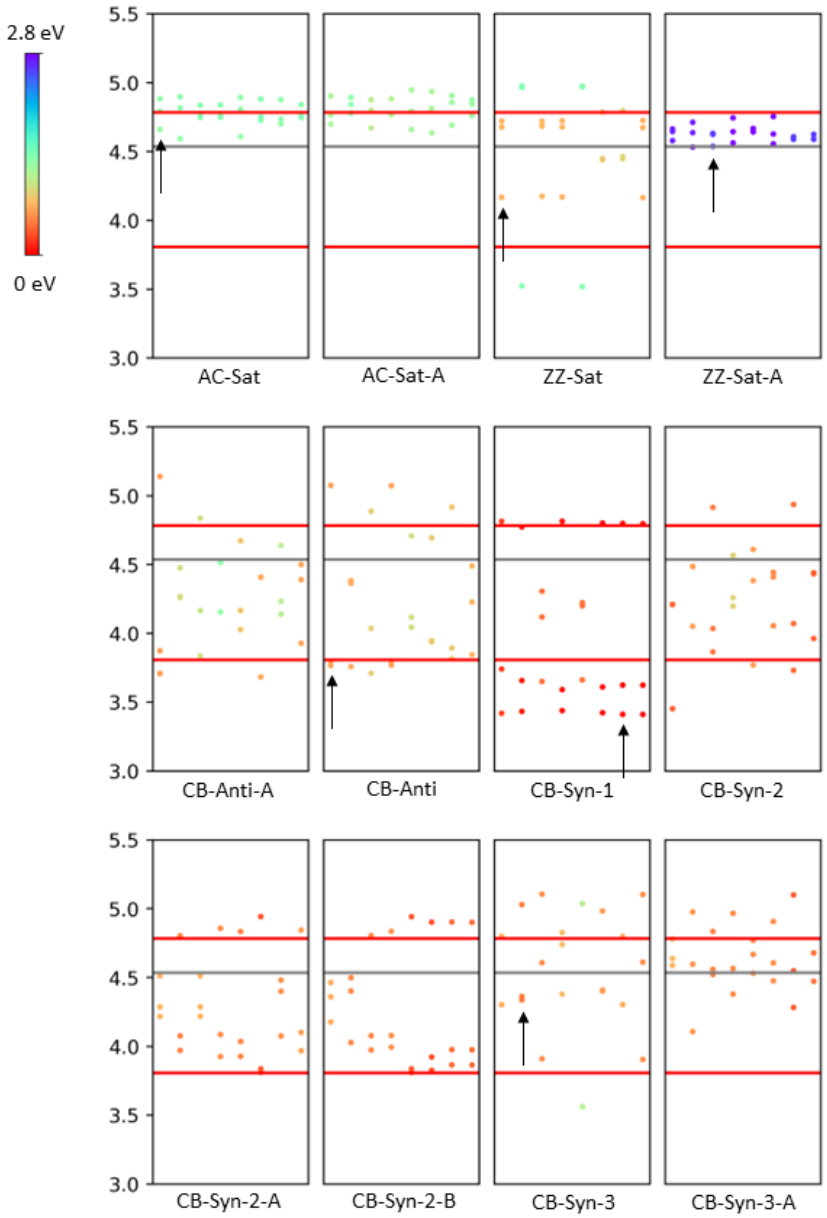

Figure S14. Packings of thread structures that start with a pre-relaxation unit cell that is 20 Å × 20 Å along the two unit cell vectors that are not along the thread direction. Each black arrows points to the lowest enthalpy packing among the same chemical species. Some chemical species, such AC-Sat-A, do not have the black arrow in this figure, because its lowest packing is found in the packing simulation that start with the experimentally derived cell in the preceding figure, instead of the 20 Å × 20 Å cell shown in the current figure. Other aspects of this figure are explained in the caption of the preceding figure.

Lowest Energy Structures, Lowest Energy Packings, and High-Pressure Decompression

Decompression data from the in situ XRD experiment (96-hour sample) was compared to the simulated diffraction, geometrically optimized through *ab-initio* computation with PBE functional,[4] DFT-D3/BJ van der Waals correction,[5, 6] and plane wave basis set, implemented in the VASP package.[7-11] All possible nanothread structures with an axial unit cell containing one or two precursor molecules without significant strain, hydrogen migration, or intramolecular bond breaking were considered. Sixteen different packing geometries were randomly generated for each thread species. After geometry relaxation, those initial packing geometries converged to one or two low-enthalpy packings for each thread species, which are then compared to the experimental *d*-spacings.

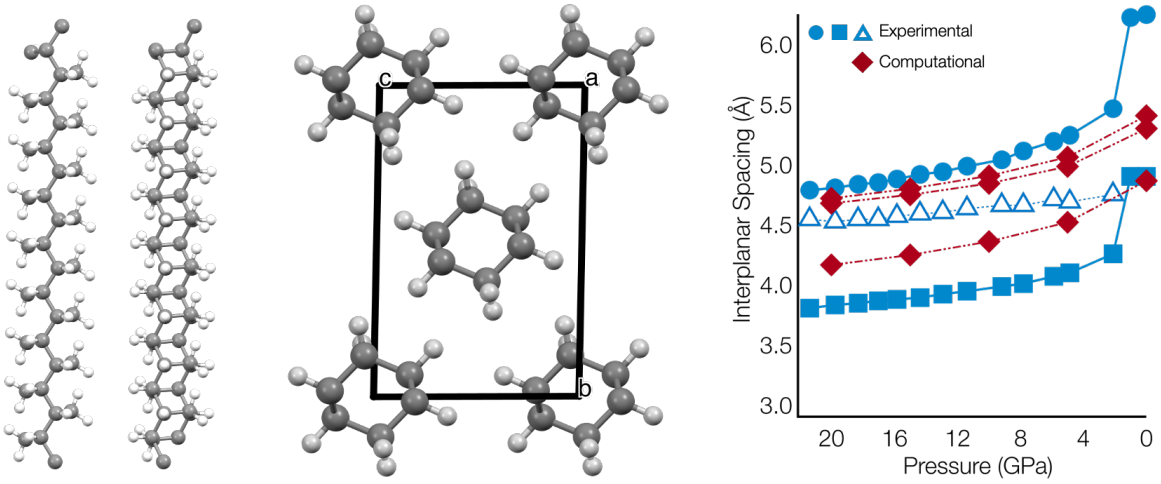

Figure S15. (left) Two side views of the AC-sat nanothread, (center) lowest energy nanothread packing, and (right) decompression of the nanothread from 20 GPa to 0 GPa. This structure is discussed in the main text.

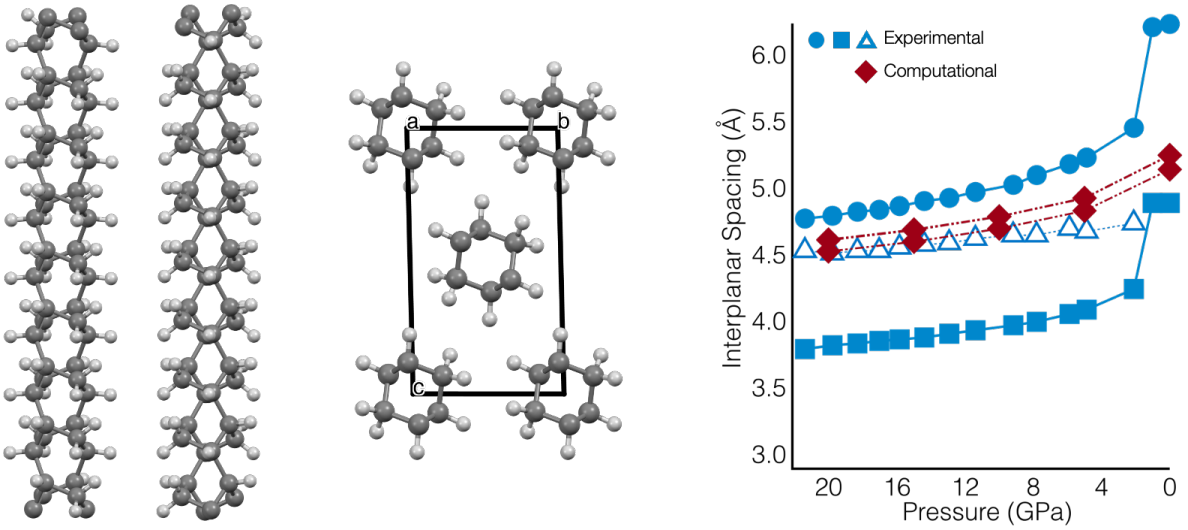

Figure S16. (left) Two side views of the AC-sat-A nanothread, (center) lowest energy nanothread packing, and (right) decompression of the nanothread from 20 GPa to 0 GPa.

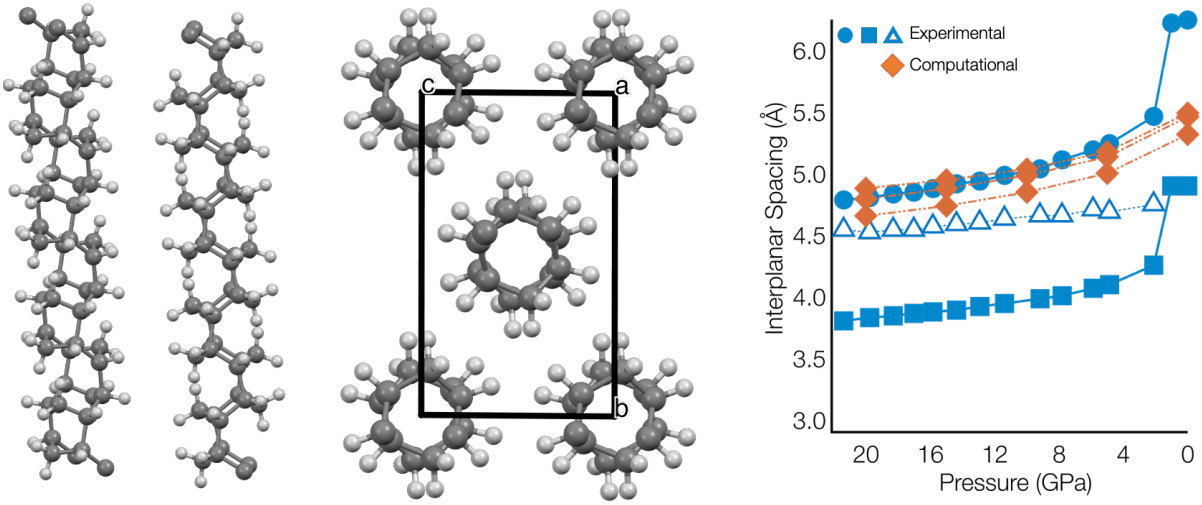

Figure S17. (left) Two side views of the ZZ-sat nanothread, (center) lowest energy nanothread packing, and (right) decompression of the nanothread from 20 GPa to 0 GPa. This structure is discussed in the main text.

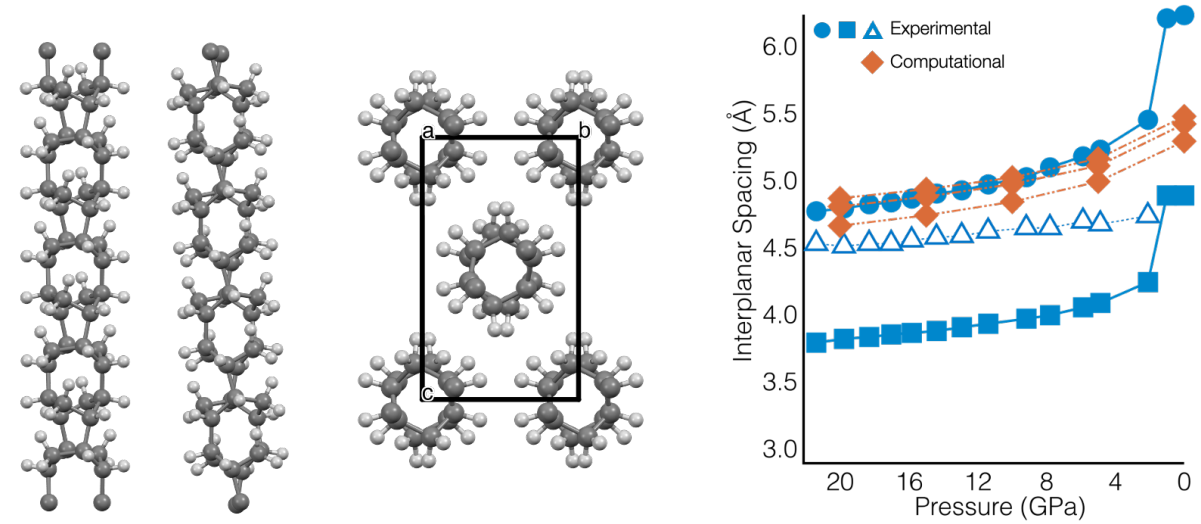

Figure S18. (left) Two side views of the ZZ-sat-A nanothread, (center) lowest energy nanothread packing, and (right) decompression of the nanothread from 20 GPa to 0 GPa.

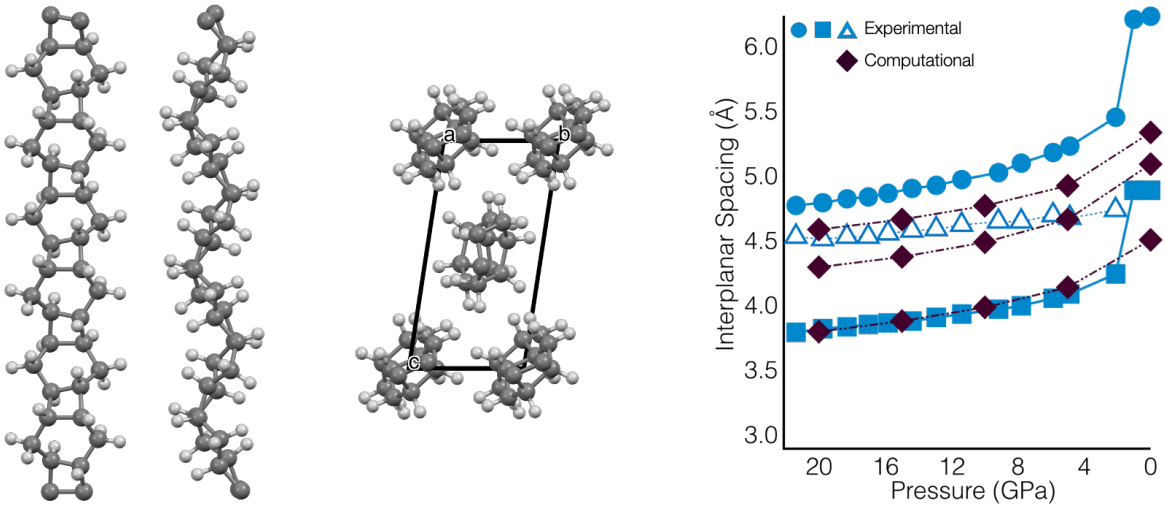

Figure S19. (left) Two side views of the CB-*Anti-A* nanothread, (center) lowest energy nanothread packing, and (right) decompression of the nanothread from 20 GPa to 0 GPa.

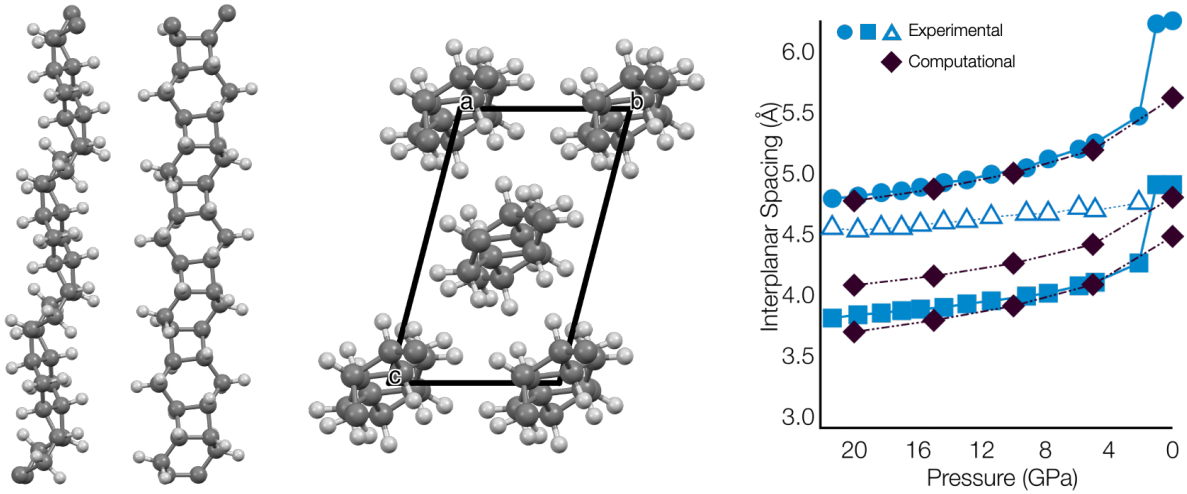

Figure S20. (left) Two side views of the CB-*Anti* nanothread, (center) lowest energy nanothread packing, and (right) decompression of the nanothread from 20 GPa to 0 GPa. This structure is discussed in the main text.

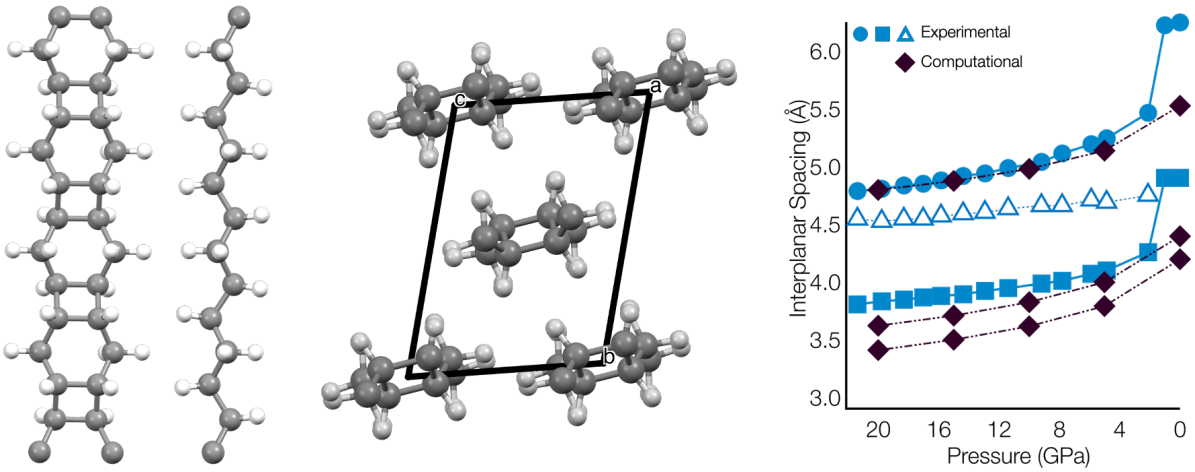

Figure S21. (left) Two side views of the CB-*Syn-1* nanothread, (center) lowest energy nanothread packing, and (right) decompression of the nanothread from 20 GPa to 0 GPa. This structure is discussed in the main text.

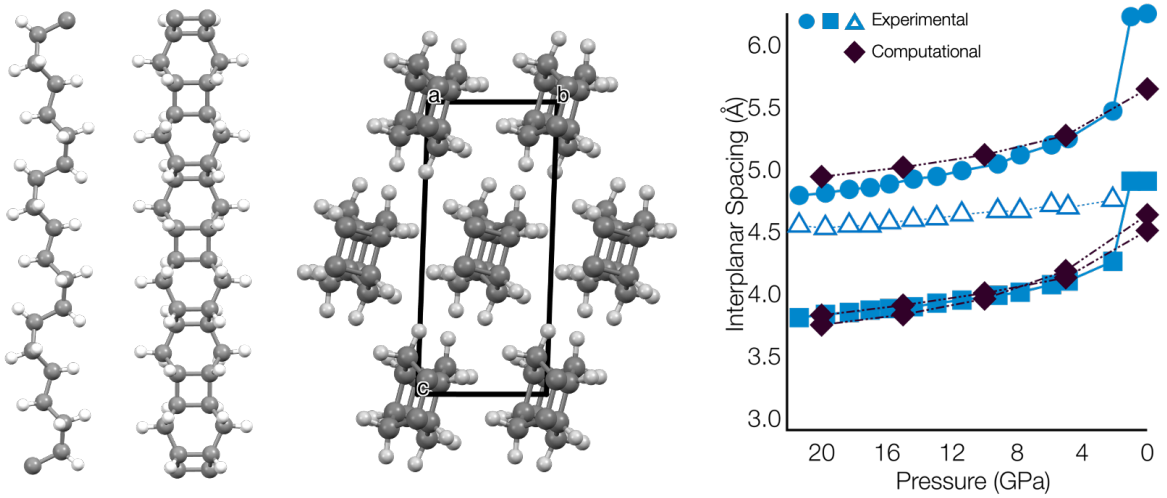

Figure S22. (left) Two side views of the CB-*Syn-2* nanothread, (center) lowest energy nanothread packing, and (right) decompression of the nanothread from 20 GPa to 0 GPa. This structure is discussed in the main text.

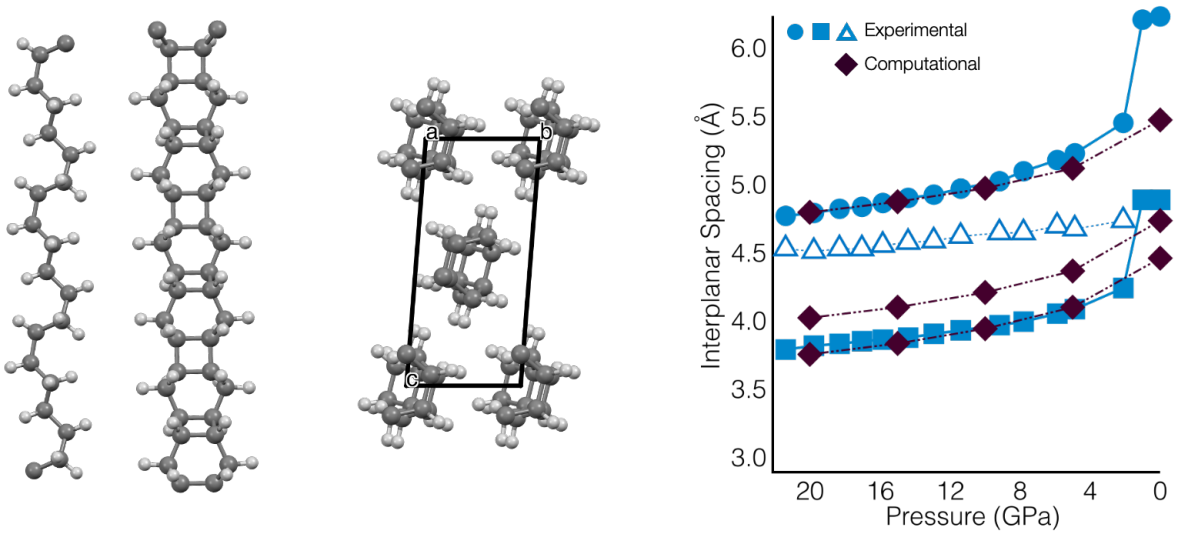

Figure S23. (left) Two side views of the CB-*Syn-2-A* nanothread, (center) lowest energy nanothread packing, and (right) decompression of the nanothread from 20 GPa to 0 GPa.

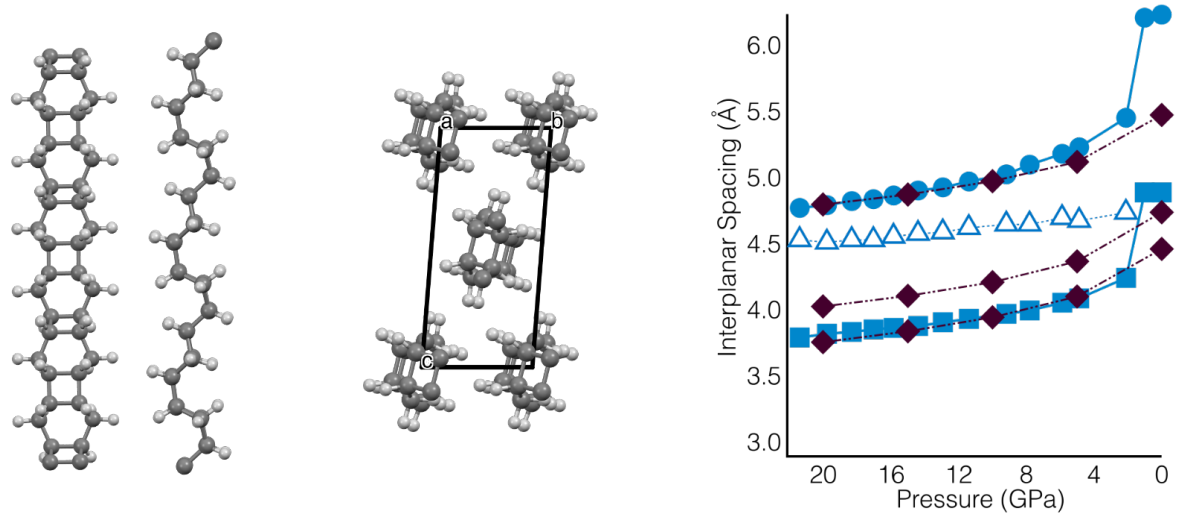

Figure S24. (left) Two side views of the CB-*Syn-2-B* nanothread, (center) lowest energy nanothread packing, and (right) decompression of the nanothread from 20 GPa to 0 GPa.

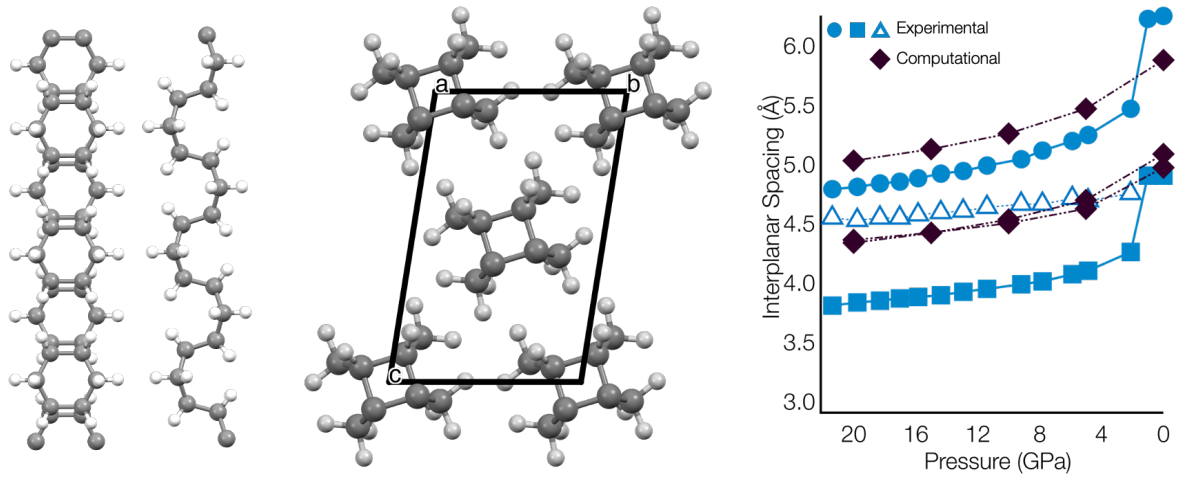

Figure S25. (left) Two side views of the CB-*Syn-3* nanothread, (center) lowest energy nanothread packing, and (right) decompression of the nanothread from 20 GPa to 0 GPa. This structure is discussed in the main text.

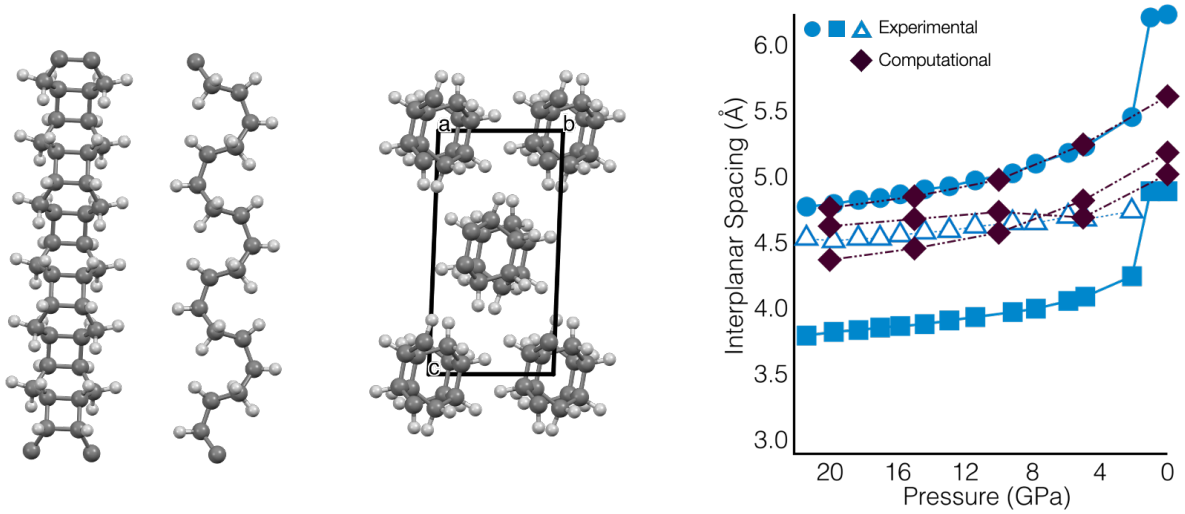

Figure S26. (left) Two side views of the CB-*Syn-3-A* nanothread, (center) lowest energy nanothread packing, and (right) decompression of the nanothread from 20 GPa to 0 GPa.

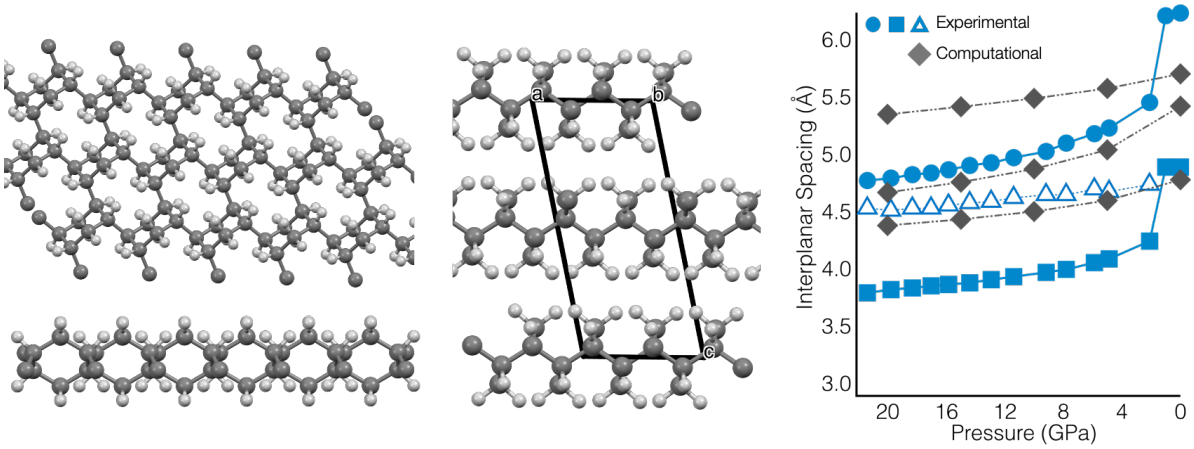

Figure S27. (left) Two side views of the ZZ-crosslinked nanothread material, (center) lowest energy nanothread packing, and (right) decompression of the nanothread from 20 GPa to 0 GPa.

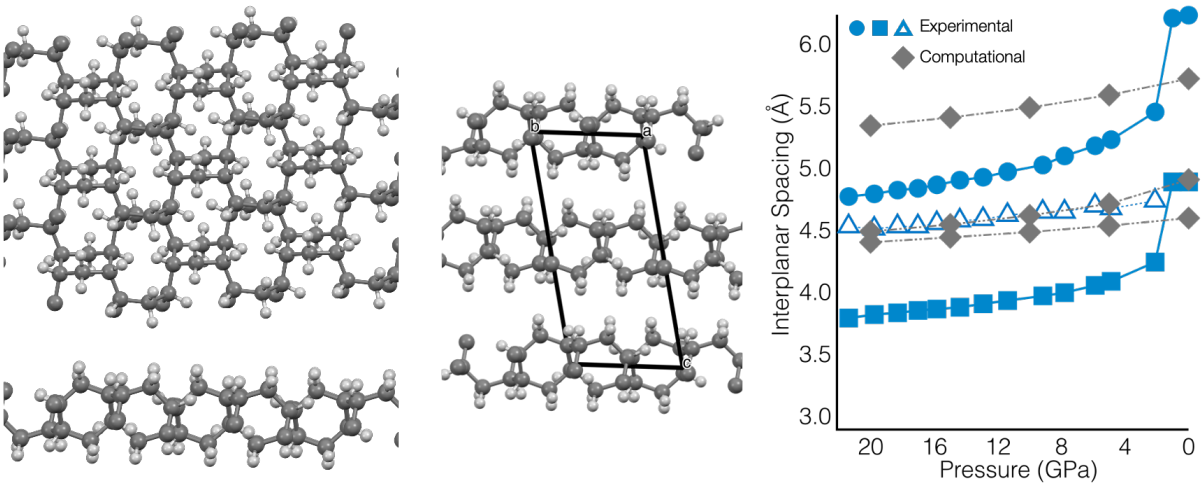

Figure S28. (left) Two side views of the AC-crosslinked nanothread material, (center) lowest energy nanothread packing, and (right) decompression of the nanothread from 20 GPa to 0 GPa.

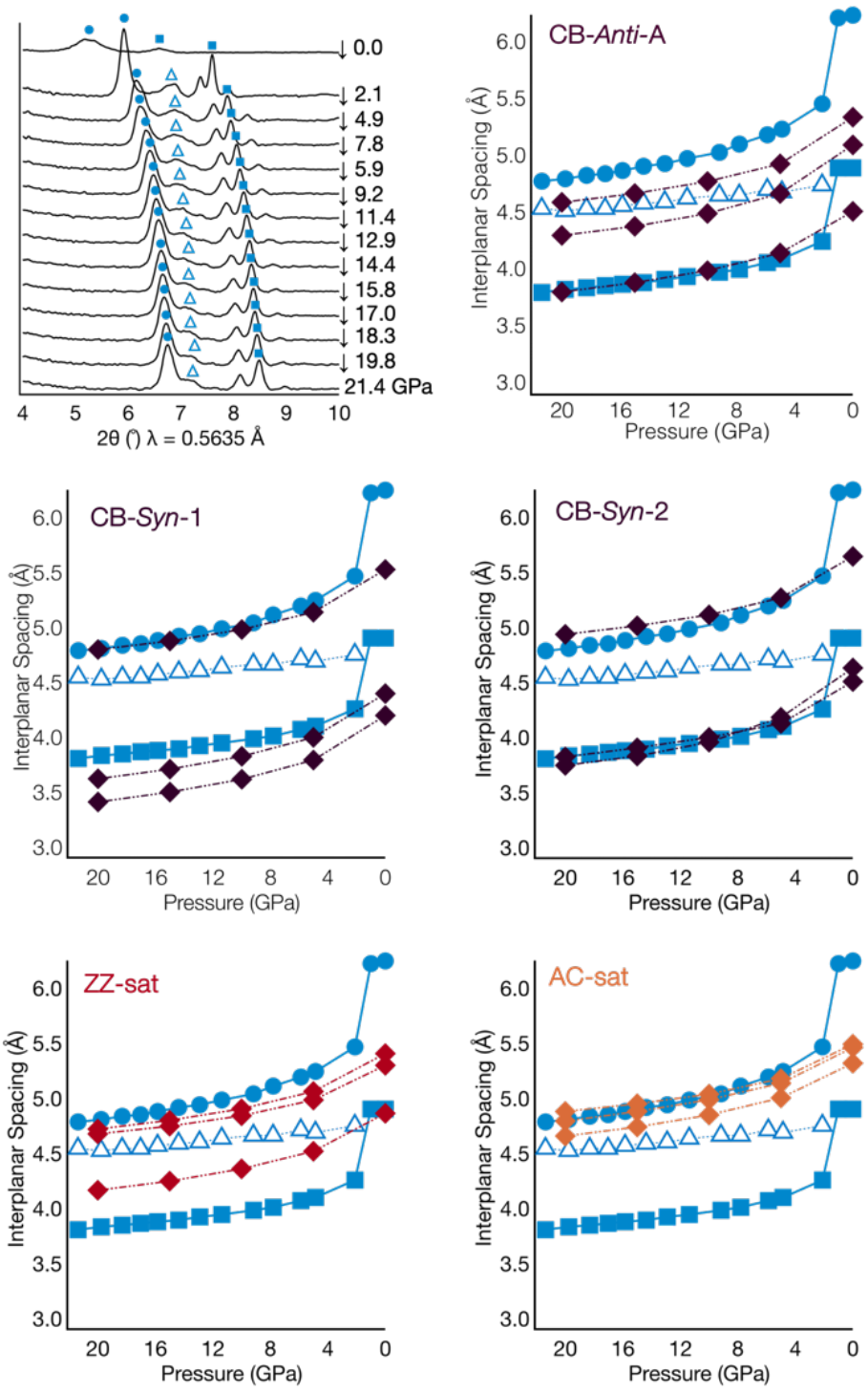

Figure S29. Experimental (96-hour sample) and simulated X-ray diffraction data for 1,4-cyclohexadiene: (top left) overlay tracing decompression with blue circles, squares, and triangles highlighting relevant peaks and comparison of experimental *d*-spacing to simulated diffraction data for different packings.

Oligomer Energies

All Gaussian16 files are uploaded to the open-access repository, figshare. They can be accessed with the following DOI, doi.org/10.6084/m9.figshare.26018272.v2.

Table S1. Energies of the optimized oligomers computed with M06-2X/6-31+G(d,p). Energies are reported in Hartrees.

Reaction	Monomer	Dimer	Trimer	Tetramer	Pentamer	Hexamer	Heptamer	Octamer
CB-Syn-1	-233.223401	-466.44845	-699.675243	-932.909867				
CB-Syn-2a	-233.223401	-466.44845	-699.675243	-932.89788				
CB-Syn-2b	-233.223401	-466.44845	-699.668946	-932.898005				
CB-Syn-2c	-233.223401	466.441485	-699.668946	-932.89788				
CB-Syn-3	-233.223401	-466.441485	-699.663621	-932.880374	-1166.098798	-1399.314792	-1632.529944	-1865.748489
CB-Anti-A	-233.223401	-466.440595	-699.645786	-932.861737				
RAD2	-233.223401	-466.35797	-699.585507	-932.812219				
RAD4	-233.223401	-466.269993	-699.482447	-932.643612	-1165.799713	-1398.947717	-1632.095755	-1865.248654
RZD2	-233.223401	-466.356012	-699.582204	-932.808782				
RZD4	-233.223401	-466.286353	-699.501744	-932.689556	-1165.872165	-1399.052302	-1632.232056	-1865.411649

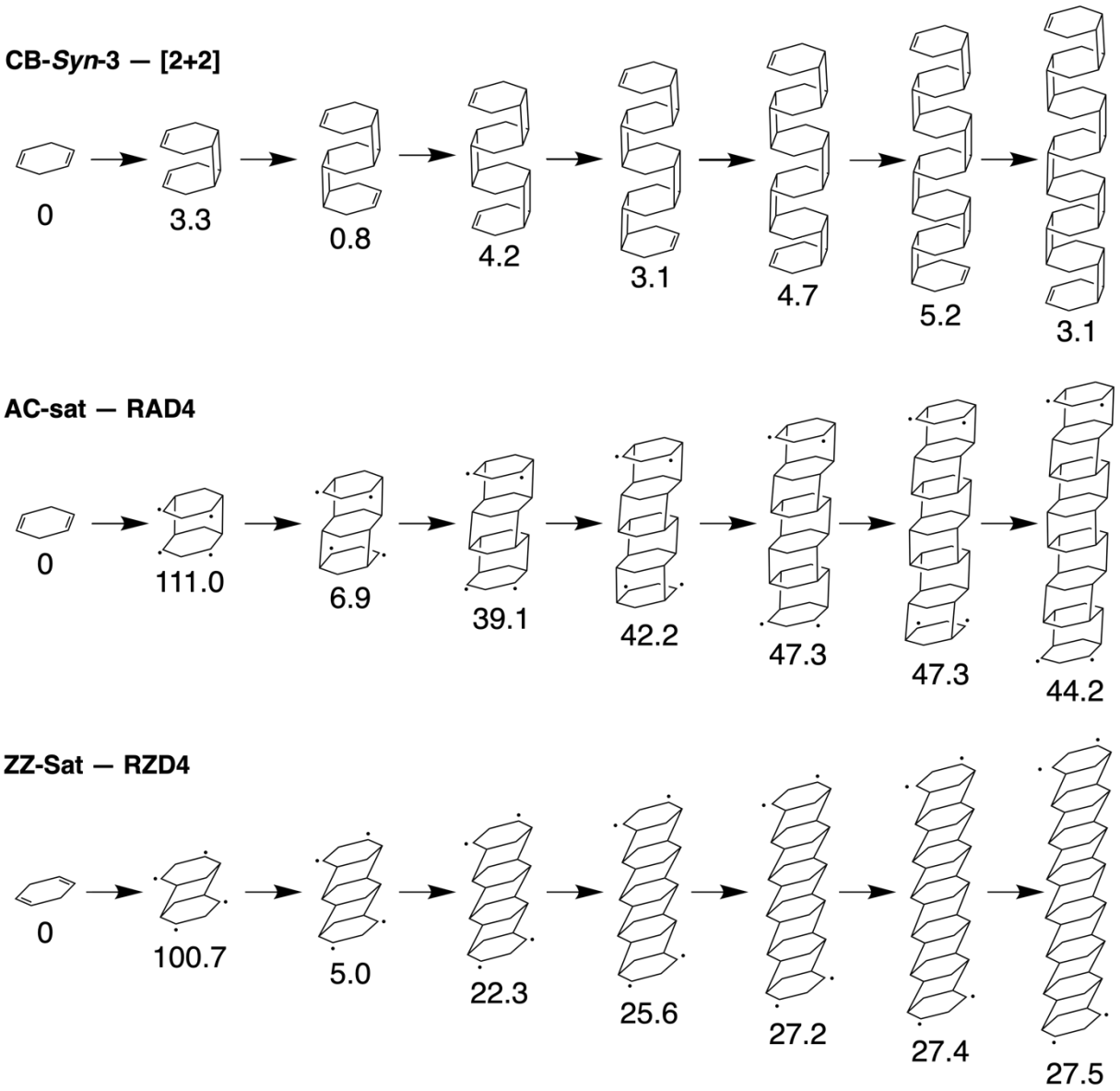

Figure S30. Reaction schemes with comparative energies listed underneath the oligomer, calculated with M06-2X/6-31+G(d,p) reported in kcal/mol.

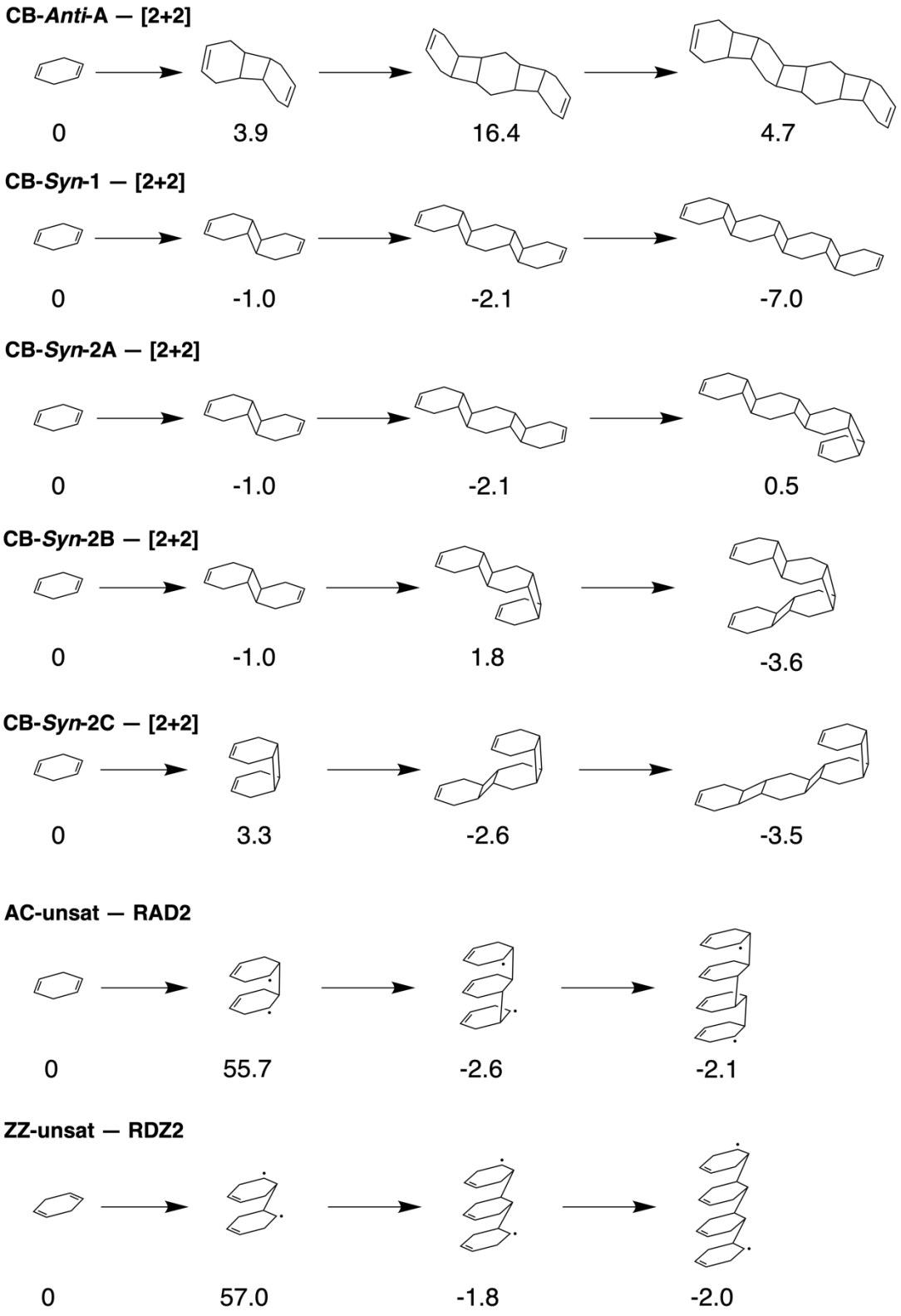

Figure S31. Reaction schemes with comparative energies listed underneath the oligomer, calculated with M06-2X/(6-31+G(d,p)) reported in kcal/mol.

Further Characterization of 1,4-Cyclohexadiene-Derived Threads

X-Ray Photoelectron Spectroscopy (XPS):

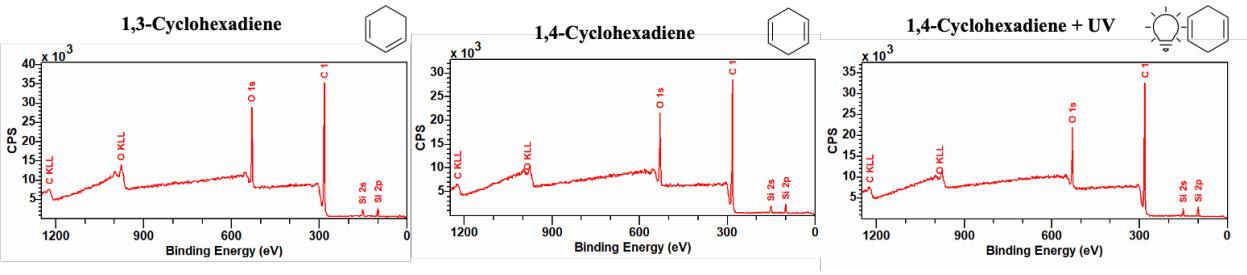

Figure S32. XPS survey scans of recovered gasket samples of 1,3-diene, 1,4-diene, and 1,4-diene with UV.

Table S2. Results of XPS Survey Scans.

Survey Scan	*C1s%*	*O1s%*
Theory	100	0
1,3-cyclohexadiene	83.9	16.1
1,4-cyclohexadiene	85.5	14.5
1,4-cyclohexadiene UV	88.2	11.8

Results of the survey scans suggest a carbon material is recovered. Additionally, the sample contains oxygen and silicon, which are not expected. The samples likely contain a polydimethylsiloxane (PDMS) contamination, which is corrected for in the overall sample content. The origin of the PDMS contamination is unknown, although we suspect it may be the result of our preparation process (e.g., sticky tack to hold gaskets in high pressure cell or glue used to hold diamond in the cell). Additional oxygen in the samples may be due to reactivity upon opening the high-pressure cell.

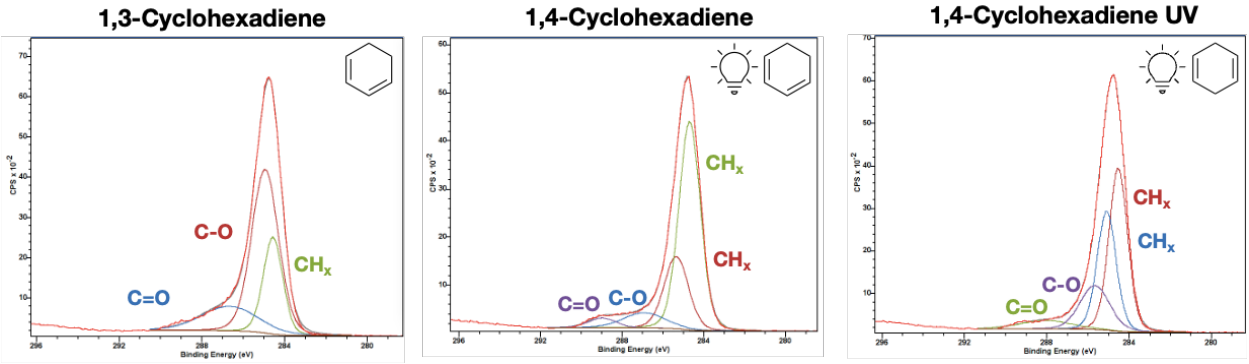

Figure S33. High resolution C1s scans.

Table S3. Results of the high resolution C1s scans.

C1s	*CHx*	*C-O*	*C=O*
Theory	100	0	0
1,3-cyclohexadiene	65.3	21.1	13.6
1,4-cyclohexadiene	87.0	9.1	3.9
1,4-cyclohexadiene UV	74.9	18.6	6.5

Adventitious carbon at 284.8 eV is completely overlapping with our sample peak. Based on the survey scans and IR spectroscopy the samples are likely reactive upon opening the high-pressure cell. The sample peaks are additionally centered between the sp^2 (284.0 – 284.5 eV) and sp^3 (284.5 – 285.0 eV) regions with features that are not easily deconvoluted. While is some cases the best fit was obtained fitting two peaks, the shits are so small they cannot be readily identified as sp^2 or sp^3.

Paris Edinburgh (PE) Press Bulk Sample Characterization of 1,4-Cyclohexadiene-Derived Threads

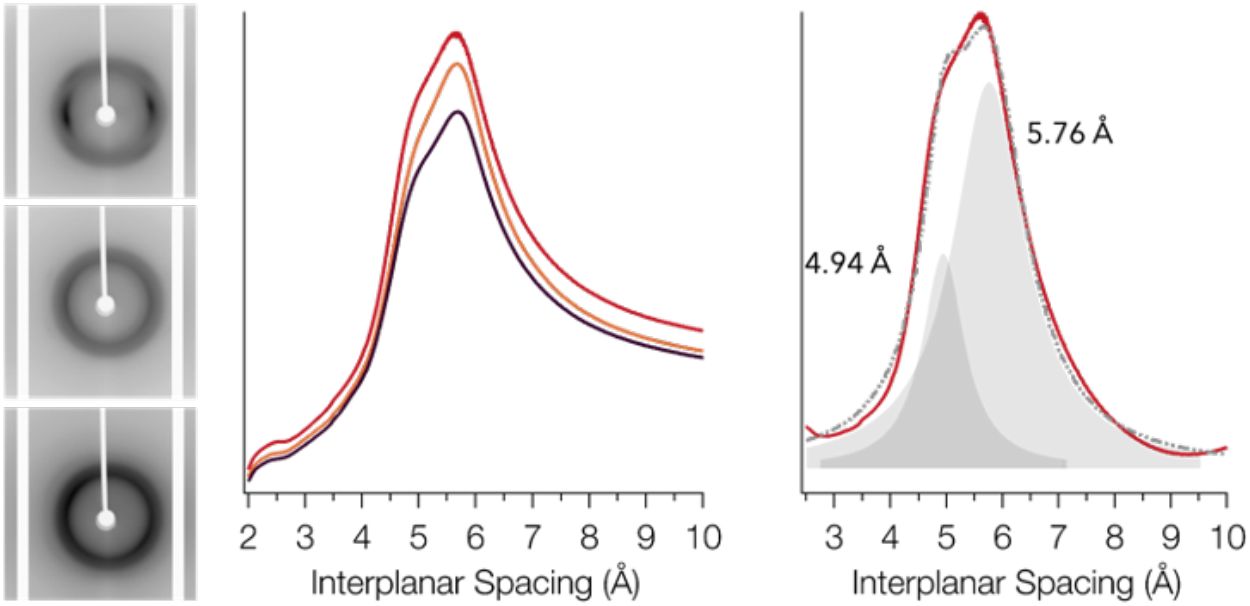

Figure S34. X-ray diffraction of the PE press sample (3 random pieces) has XRD consistent with other recovered thermal samples, the combined of which suggest the packing of the thermally meditated polymerization product is ill-defined. While consistent with other thermal samples from DAC experiments, this is distinct from the photochemical experiments. See summary table of *d*-spacings below.

Table S4. Summary of the recovered *d*-spacings from the thermally and photochemically mediated polymerizations of 1,4-cyclohexadiene.

24-hour (DAC)	96-hour (DAC)	24-hour (PE press)	Photo (DAC)
6.04 Å	6.14 Å		6.24 Å
5.83 Å		5.76 Å	
			5.04 Å
	4.90 Å	4.94 Å	4.86 Å

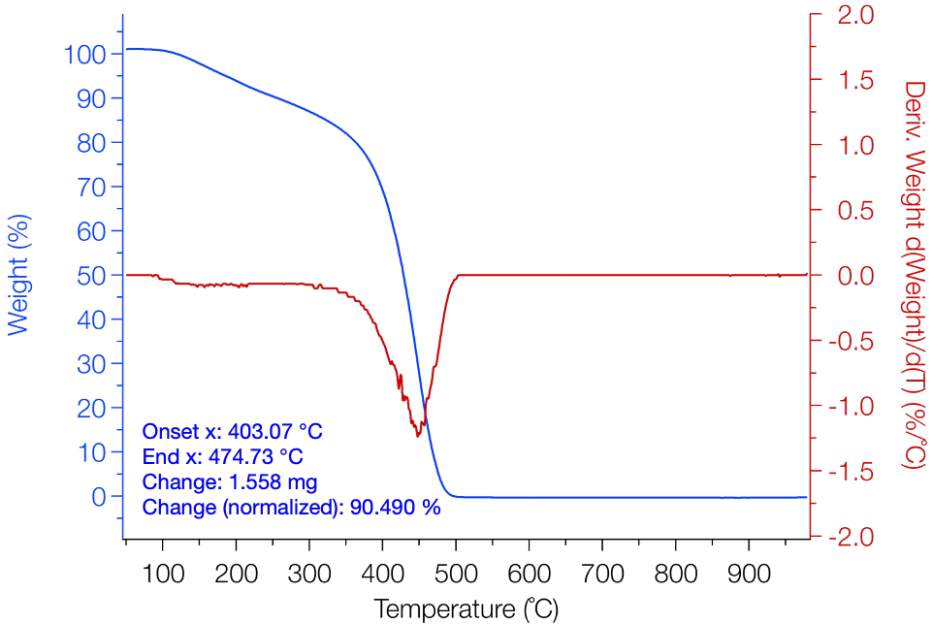

Figure S35. TGA curve resulting from the PE press sample (blue) and the first derivative (red).

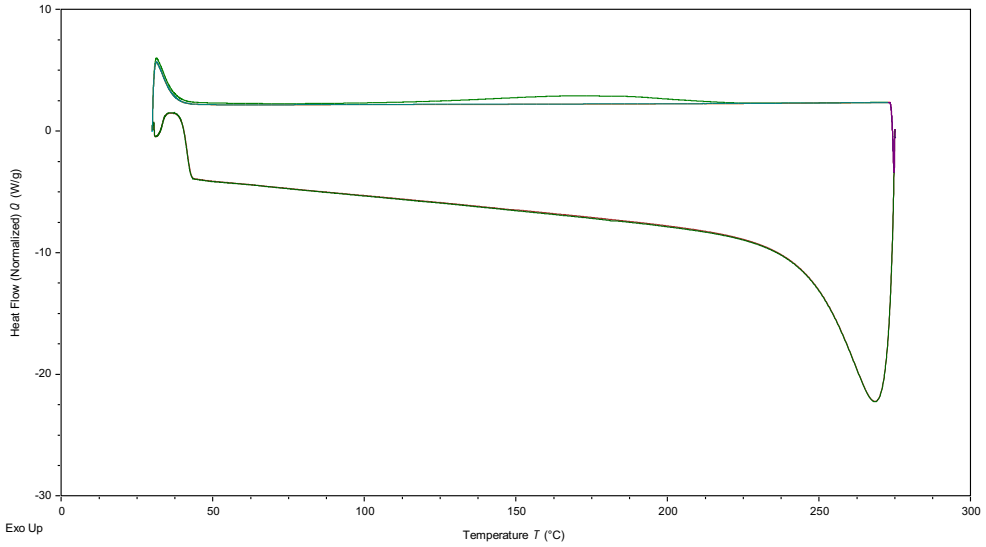

Figure S36. DSC curves resulting from the PE press sample measured over 3 cycles.

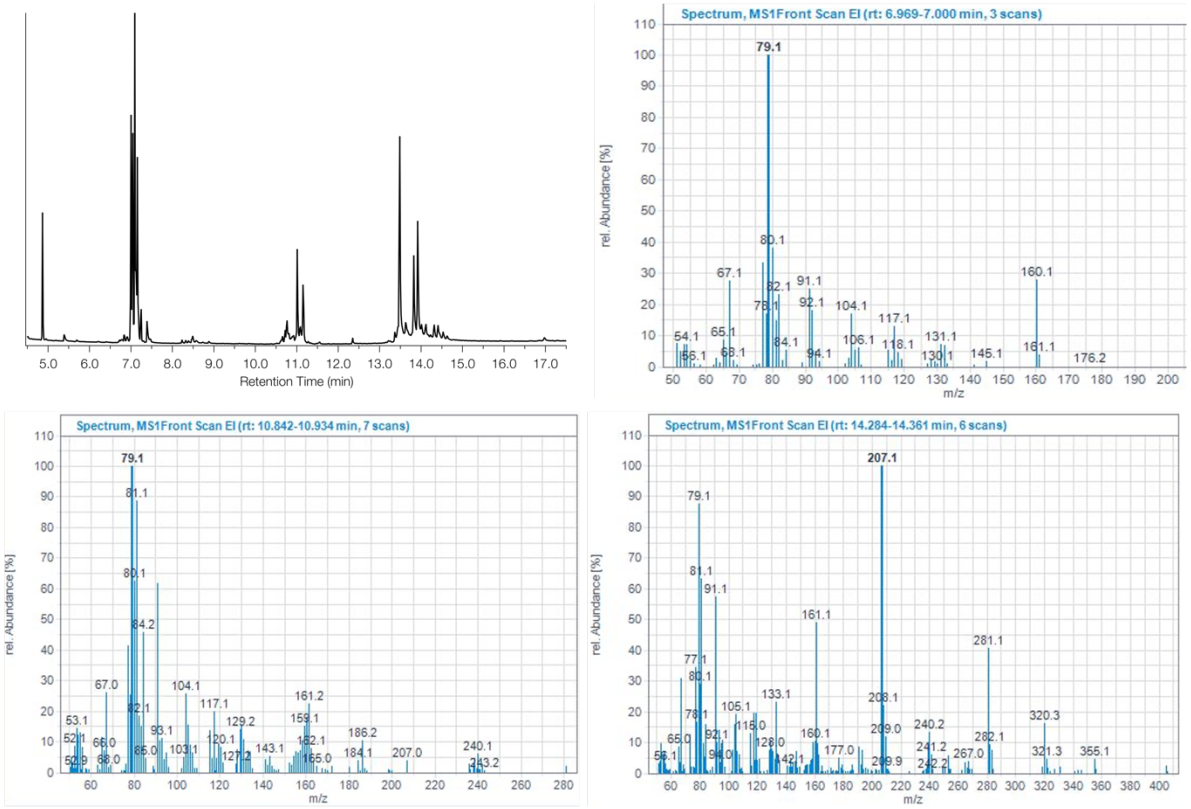

Figure S37. GC-MS traces obtained from soluble portion of PE press sample. Cyclohexadiene dimers (160.1 m/z), trimers (240.2 m/z), and tetramers (320.3 m/z) are observed as part of the sample.

References

(1) Prescher, C.; Prakapenka, V. B. DIOPTAS: a program for reduction of two-dimensional X-ray diffraction data and data exploration. *High Press. Res.* **2015**, *35* (3), 223-230.
(2) Seah, M. P. Summary of ISO/TC 201 Standard: VII ISO 15472 : 2001—surface chemical analysis—x-ray photoelectron spectrometers—calibration of energy scales. *J. Surf. Interfac.* **2001**, *31* (8), 721-723.
(3) Ciabini, L.; Santoro, M.; Bini, R.; Schettino, V. High pressure reactivity of solid benzene probed by infrared spectroscopy. *J. Chem. Phys.* **2002**, *116* (7), 2928-2935.
(4) Perdew, J. P.; Burke, K.; Ernzerhof, M. Generalized Gradient Approximation Made Simple. *Phys. Rev. Lett.* **1996**, *77* (18), 3865-3868.
(5) Grimme, S.; Antony, J.; Ehrlich, S.; Krieg, H. A consistent and accurate ab initio parametrization of density functional dispersion correction (DFT-D) for the 94 elements H-Pu. *J. Chem. Phys.* **2010**, *132* (15), 154104.
(6) Grimme, S.; Ehrlich, S.; Goerigk, L. Effect of the damping function in dispersion corrected density functional theory. *J. Comput. Chem.* **2011**, *32* (7), 1456-1465.
(7) Kresse, G.; Joubert, D. From ultrasoft pseudopotentials to the projector augmented-wave method. *Phys. Rev. B* **1999**, *59* (3), 1758-1775.
(8) Kresse, G.; Hafner, J. Norm-conserving and ultrasoft pseudopotentials for first-row and transition elements. *J. Condens. Matter Phys.* **1994**, *6* (40), 8245.
(9) Kresse, G.; Hafner, J. Ab initio molecular dynamics for liquid metals. *Phys. Rev. B* **1993**, *47* (1), 558-561.
(10) Kresse, G.; Furthmüller, J. Efficiency of ab-initio total energy calculations for metals and semiconductors using a plane-wave basis set. *Comput. Mater. Sci.* **1996**, *6* (1), 15-50.
(11) Kresse, G.; Furthmüller, J. Efficient iterative schemes for ab initio total-energy calculations using a plane-wave basis set. *Phys. Rev. B* **1996**, *54* (16), 11169-11186.